34th Annual International Conference of the IEEE EMBS
San Diego, California USA, 28 August - 1 September, 2012

An Ideal Observer Approach to Mechanical Limits in B-Mode Ultrasound Imaging*

Craig K. Abbey, Nghia Q. Nguyen, William D. O'Brien Jr., and Michael F. Insana, *Member, IEEE*

Abstract— **In medical applications, the amplitude of ultrasonic pulses is often constrained by mechanical considerations summarized by a mechanical index. We apply the ideal observer approach in a simulation environment to evaluating the role of mechanical index limits on task performance in b-mode ultrasonic imaging. We simulate a linear array operating at 15MHz and 60% fractional bandwidth, and consider three tasks related to breast sonography at a depth of 4cm. The ideal observer suggests that there are gains in performance – and hence the quantity of diagnostic information – as the limit on mechanical index is raised. However these gains are almost completely erased after computation of a standard b-mode envelope.**

I. Introduction

The goal of medical ultrasonic imaging is to support accurate decisions involving patient diagnosis and treatment, and this constitutes the ultimate measure of imaging-system performance. However, clinical evaluation of performance is generally costly and time consuming, and therefore ill-suited to fine tuning of imaging systems and imaging methodology. It is also possible to characterize imaging system in terms of engineering parameters such as contrast, resolution, and noise. But these often trade off against each other, resolution vs noise for example, and the connection to clinical performance is not always clear.

We have been developing the ideal observer in ultrasound as a bridge between these two approaches to image system design and optimization. The ideal observer uses imaging data to perform a task in a statistically optimal way [1-3], and thus achieves the highest possible ensemble performance. Simple and abstracted tasks are used in simulation studies to make the computations tractable [1, 4-6]. An example of such tasks is detection of a low-contrast hypo-echoic lesion against a uniform scattering background. Engineering parameters directly influence the statistical properties of the imaging data, which in turn impact task performance of the ideal observer. Since the ideal observer optimizes performance, we can use its performance as a measure of diagnostic information content, that is, how much information is available in the data to perform the task. Furthermore, we can evaluate the ideal observer at various stages in the process of forming a final image to see where information is lost. We have used the approach previously to investigate signal processing [1, 6], beamforming [4], and pulse shape [5] in b-mode imaging.

In this study we use the ideal observer approach to investigate how the amplitude of the transmitted pressure pulse in an ultrasonic system changes the diagnostic information available in the scan. Pulse amplitude is a direct consequence of the transmitted power [7], which is typically limited by mechanical and thermal constraints. However, these constraints are formulated on the principle of avoiding harmful bioeffects in a worst case scenario [8]. To our knowledge, there has been no task-based evaluation of what possible limitations such constraints impose on the transfer of diagnostic information in the subsequent images [9].

The tasks we investigate simulate the use of ultrasound as an adjunct to mammography in breast-cancer screening and diagnosis. We consider detection of a low-contrast hypo-echoic lesion, discrimination of an indistinct lesion boundary, and detection of echogenic material inside a defined lesion. In breast sonography, mechanical limits are generally reached well before thermal limits, and so we will focus of mechanical limits, expressed as a mechanical index (MI). FDA guidelines recommend that MI not exceed 1.9 [8, 10]. We investigate the effect of increasing MI from the current standard of 1.9 to a somewhat higher value of 2.5.

II. Theory

The basic approach for this work has been developed previously [1] and will be only briefly reviewed given the page limits of this proceedings paper. The fundamental assumption is that incoherent scattering from tissue can be modeled as a Gaussian stochastic process where the relevant information for performing a task is encoded in the variance map (i.e. the variance of the process at each spatial point).

A. Ideal Observer

Let the vector $\mathbf{f}$ represent the sampled reflectivity of the object. In a simple (2-class) task, this vector is presumed to be drawn from one of two probability density functions

$$\begin{aligned} &\text{Signal Absent: } \mathbf{f} \sim \mathrm{MVN}\left(\mathbf{0}, \sigma_{\mathrm{Obj}}^2\left(\mathbf{I}+\mathbf{S}_0\right)\right) \\ &\text{Signal Present: } \mathbf{f} \sim \mathrm{MVN}\left(\mathbf{0}, \sigma_{\mathrm{Obj}}^2\left(\mathbf{I}+\mathbf{S}_1\right)\right) \end{aligned} \quad (1)$$

with the different class variance maps represented by the diagonal matrices $\mathbf{S}_0$ and $\mathbf{S}_1$. These represent the deviation from equal-variance white noise, and the differences between

*Research supported by NIH R01- CA118294.

C. K. Abbey is with the Dept. of Psychological and Brain Sciences at U.C. Santa Barbara, CA 93106 (phone: 805-893-3853; fax: 805-893-4303; e-mail: abbey@psych.ucsb.edu).

N. G. Nguyen, W. D. O'Brien Jr., and M.F. Insana are with the Dept.s of Bioengineering and Electrical and Computer Engineering at the Unversity of Illinois, Urbana-Champaign, IL 61801 USA. (respective e-mails: nnguyen6@illinois.edu, wdo@illinois.edu, mfi@illinois.edu).

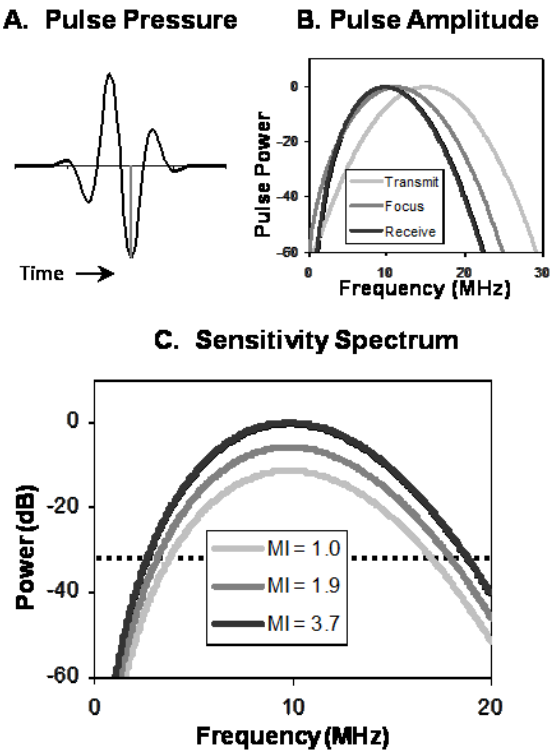

Figure 1. System Characterization. The pulse pressure profile at focus (A) is shown with vertical line indicating peak rarification pressure. Normalized pulse spectra are shown (B) for transmission, focus, and receive. Received spectra (C) are shown for different mechanical Index (MI) values along with noise power.

$\mathbf{S}_1$ and $\mathbf{S}_0$ are the sole basis for discriminating between the two classes.

The RF signal, **g**, is well modeled as a noisy linear transformation of the object reflectivity function. Let **H** represent the system matrix and **n** represent acquisition noise, then

$$\mathbf{g} = \mathbf{H}\mathbf{f} + \mathbf{n}\,. \qquad (2)$$

An envelope image is generated from the RF by using a Hilbert transform to form the analytic signal (**A**), and then taking the element-by-element magnitude. Often downsampling is part of the envelope formation though we have not included that in our model. We will also investigate the effect of a Wiener filter (**W**) applied to the RF before computing the analytic signal. The resulting envelope image is defined as

$$\mathbf{e}_{\mathrm{Std}} = \left|\mathbf{A}\mathbf{g}\right|, \text{ or } \mathbf{e}_{\mathrm{WF}} = \left|\mathbf{A}\mathbf{W}\mathbf{g}\right| \qquad (3)$$

respectively.

The ideal observer for simple two-class tasks of the sort described by Eq. 1, is defined in terms of the log-likelihood ratio (LLR) for the two class probability density functions. Following earlier works [1, 3, 4], we can define the ideal observer at various stages of the image-formation process, ranging from the object itself (at a given sampling rate), the RF signal, or the final envelope image. For the sampled object function or the RF signal, the LLR can be computed explicitly. For envelope detected images, the LLR is approximated using the approach of Smith and Wagner [11]. Evaluating the ideal observer consists of applying the log-likelihood ratio test statistic to Monte-Carlo samples from the stage of interest.

B. System Model

The system model represented by **H** in Eq. 2 above is implemented assuming a linear array with a Gaussian transmitted pulse amplitude at a center frequency (f_c) of 15MHz. The model assumes 192 elements in the transmission aperture at 0.2 mm per element with 1.0mm elevation. The transmitted pulse is propagated into the far field and back to the transducer by Rayleigh-Sommerfeld diffraction theory. We also assume attenuation similar to that measured in breast tissue at 0.75 dB/MHz/cm, and frequency dependent reflectivity as a power-law proportional to $f^{1.2}$. The pulse amplitude is given as a function of frequency by

$$P_T(f) = P_0 e^{-\frac{1}{2}\left(\frac{f-f_c}{a}\right)^2} \qquad (4)$$

where P_0 is the pulse amplitude and the bandwidth constant, a, which ensures the FWHM of the pulse amplitude is 60% of the center frequency. Propagation to the focal point at 4cm gives the temporal waveform, $P_{\mathrm{Foc}}(t)$, that is used to determine the mechanical index of the pulse as

$$\mathrm{MI} = \frac{\max\left(P_{Amb} - P_{\mathrm{Foc}}(t)\right)}{\sqrt{f_c}}. \qquad (5)$$

where the numerator is the peak rarification pressure of the pulse at focus. To achieve a given MI, we adjust the free parameter P_0 in Eq. 4 by simulating propagation in water with subsequent derating by 0.3 dB/MHz/cm, consistent with laboratory measurements of MI [8].

Fig. 1 shows some properties of the simulated system for a 15 MHz pulse at 60% fractional bandwidth. Fig. 1A shows the pressure waveform at focus indicating the peak rarification pressure. Fig. 1B shows how propagation, attenuation, and reflectivity modify pulse the pulse frequency spectrum going from transmission to focus and then to receive. The primary effect is a drop in center frequency due to attenuation. Fig. 1C shows how increasing the MI increases the power spectrum of the pulse received after scattering at the focal point.

III. Methods

Our study consists of evaluating three tasks related to discriminating malignant and benign abnormalities in breast sonography as the mechanical index of the pulse changes from 1.9 to 2.5 over a range of 3 to 15 MHz at 60% fractional bandwidth. Example envelope images of the tasks considered are shown in Fig. 2, although the tasks are shown at exaggerated contrast (i.e. easier to discriminate) than for the results given. The tasks are numbered 1, 3, and 5 for consistency with prior works [1, 4-6]. Task 1 is detection of a mild hypo-echoic lesion. The feature of interest is the dark region in the shape of a 6mm diameter lesion. Task 3 involves discriminating a smooth indistinct boundary from a well-circumscribed boundary in a high contrast lesion. Here the feature of interest is the "fuzziness" of the boundary.

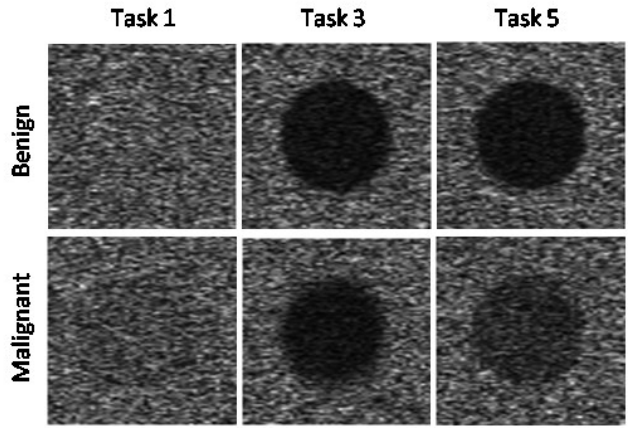

Figure 2. Example Images. Images (at 15MHz and 60% fractional bandwidth) in each of the malignant/benign discrimination tasks are shown cropped to emphasize the central area of the image. The differences between the classes are exaggerated here to emphasize the features of interest.

Task 5 is discrimination of echogenic material in the interior of a high-contrast lesion. Here the feature of interest is a brighter lesion interior.

Ideal observer performance was evaluated for the sampled object (where mechanical index is not relevant since there is no pulse yet), the RF signal, the standard envelope image, and a Wiener filtered envelope image. In each case 2,000 Monte-Carlo images were evaluated in each class. Performance was evaluated by estimating the area under the ROC curve from the log-likelihood ratio test statistics derived from each sample. This process was repeated several times adjusting the parameters of the task in order to find the parameters that produced 80% correct (i.e. AUC = 0.8). The measure of performance is then the threshold contrast, defined as deviation in variance maps

$$C = \Delta x \Delta z \sum_j \left| S_1[j,j] - S_0[j,j] \right|, \qquad (6)$$

where $S_0[j,j]$ and $S_1[j,j]$ are the diagonal elements of the $\mathbf{S}_i$ matrices defined in Eq. 1. Note that better performance results in a lower contrast threshold. Task efficiency is then computed as the squared ratio of the threshold contrast of the sampled object to the threshold contrast of the RF or envelope data. For example, task efficiency of the RF data for a given task is

$$\eta_{\mathrm{RF}} = \left(\frac{C_{\mathrm{Obj}}}{C_{\mathrm{RF}}} \right)^2 . \qquad (7)$$

Analogous expressions are used for the envelope images.

IV. Results and Discussion

The results of this study are shown in Fig. 3, where task efficiency is plotted as a function of Center frequency for MI values of 1.9 and 2.5. The range of efficiency is highly task dependent, with maximum RF efficiency in Task 1 at nearly 40%, and in Task 5 at less than 2%. Efficiency generally increases with center frequency with the exception of the highest frequencies in task 5. Efficiency is highest for RF

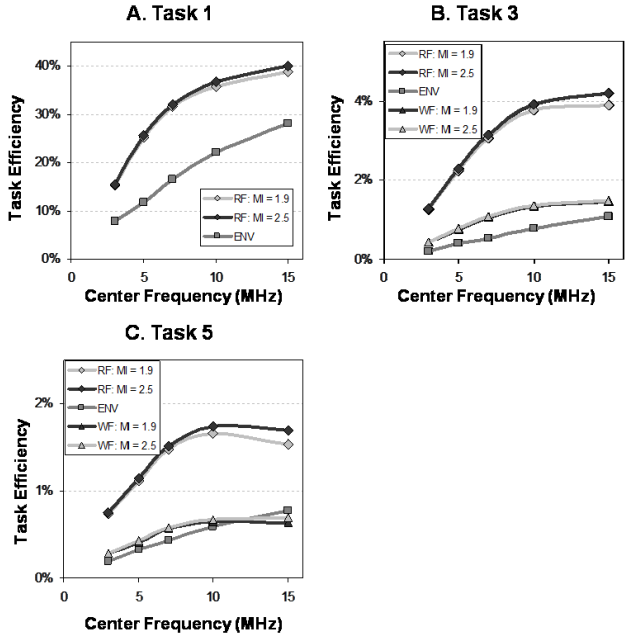

Figure 3. Efficiency results. Efficiency (relative to the sampled object) is shown for RF signals, standard b-mode envelope images (ENV) and Wiener-filtered envelope images (WF) as a function of transmitted center frequency at MI of 1.9 and 2.5 in each task (A-C). Note that for ENV images, the plot symbols for the MI values are indistinguishable, and hence only one plot is shown. Also in Task 1 the WF and RF plots were indistinguishable (for each MI value), and hence only the RF plots are shown.

signals, which is understandable since the b-mode and Wiener-filtered envelope images are derived from the RF, and hence cannot increase diagnostic information. The difference in efficiency across MI is most pronounced for RF signals at 15 MHz. The b-mode envelope images (evaluated under Smith-Wagner approximations to the ideal observer) show substantially lower overall efficiency relative to the RF signals. In this case, the difference due to MI is so small that the plots overlap each other and cannot be distinguished. Thus any additional information added to the RF signal as a result of increasing the MI is subsequently lost in the computation of a standard b-mode envelope. The Wiener filtered envelopes are virtually identical to the RF ideal observer in Task 1, but substantially lower in Tasks 3 and 5. The WF envelopes have higher efficiency than the standard b-mode envelopes except at the highest center frequencies of Task 5. They generally have smaller differences from increased MI at 15 MHz than the RF signals, but they can be discerned, particularly in Task 5.

Looking at the plots in Fig. 3, it is not clear if increases with mechanical index represent large or small changes in performance. As a way to give context to the improvements, we compare them to changes in efficiency due to the center frequency of the pulse. To do this we compute the relative change in efficiency per unit MI going from MI values of 1.9 to 2.5 at 15MHz,

$$G_{\mathrm{MI}} = \frac{\eta_{\mathrm{MI=2.5}} - \eta_{\mathrm{MI=1.9}}}{\eta_{\mathrm{MI=1.9}} (2.5 - 1.9)} . \qquad (8)$$

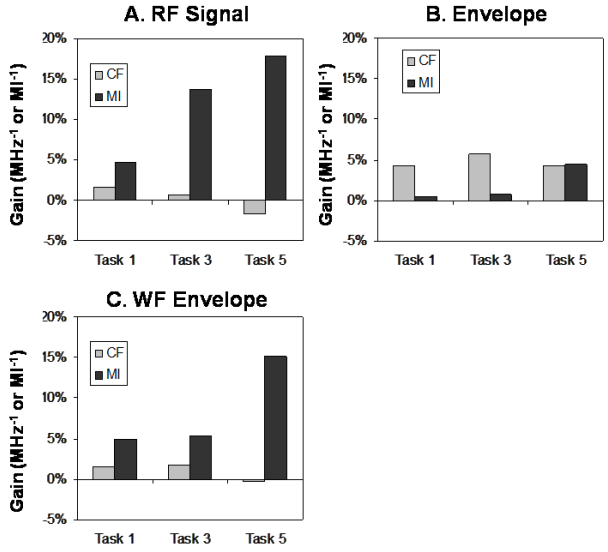

Figure 4. Efficiency Gains. The relative change in efficiency per unit of center frequency or MI are plotted for RF signals (A), standard b-mode envelope images (B) and Wiener-filtered envelope images (C) across tasks.

We also compute the relative change in efficiency per unit center frequency going from center frequency values of 10 MHz to 15 MHz at MI of 1.9,

$$G_{CF} = \frac{\eta_{CF=15} - \eta_{CF=10}}{\eta_{CF=15}(15-10)}. \qquad (9)$$

Each of these can be thought of as an efficiency gain for mechanical index or center frequency.

Fig. 4 plots the gains across tasks for the RF signals (A) and the two envelope images (B,C). In the RF data, the CF gain for Task 1 is 1.6% compared to 4.7% for the MI gain. This suggests that a unit increase in MI is equivalent to approximately a 2.9MHz increase in center frequency. This effect is more pronounced in Task 3 due to the smaller CF gain and larger MI gain. In Task 5 the CF Gain is negative, since efficiency is going down with increased center frequency, making it a poor yardstick for performance improvements. For the b-mode envelope images, we see that the MI gains are small compared to CF, except in Task 5 where generally low overall efficiency mean that small improvements in efficiency with MI (0.75% to 0.77%) are relatively larger. Higher levels of MI gain are found in the Wiener filtered envelopes, which shows that envelope computation does not necessarily negate additional information from a higher limit on mechanical index.

V. Conclusion

The study reported here has demonstrated that diagnostic information in the acquired RF data increases with mechanical index at high transmit center frequency (15 MHz). At lower center frequencies, there was little improvement, suggesting little value to increasing MI for the discrimination tasks considered here. At 15 MHz, the MI induced increases in performance are task dependent, with higher gains for high-contrast discrimination tasks than a low-contrast detection task. Thus the improvements in diagnostic information found by increasing MI are dependent on the properties of the pulse and the diagnostic task under consideration.

However, nearly all of these gains in information are negated when a standard envelope image is created from the RF. In addition to a substantial overall loss of information compared to the RF, the envelope removes almost all evidence for a trend in improved performance with greater mechanical index. Therefore evaluations of mechanical index on the basis of standard envelope images will give the appearance that performance has flattened with mechanical index suggesting that it is unimportant. When a more elaborate envelope computation is used, involving a Wiener filter applied to the RF before envelope computation, performance retains some dependence on mechanical index. On the basis of these findings, there is little point in modifying the limit on mechanical index unless the envelope computation is modified as well.

VI. References

[1] C. K. Abbey, R. J. Zemp, J. Liu, K. K. Lindfors, and M. F. Insana, "Observer efficiency in discrimination tasks simulating malignant and benign breast lesions imaged with ultrasound," *IEEE Trans Med Imaging,* vol. 25, pp. 198-209, Feb 2006.

[2] R. J. Zemp, C. K. Abbey, and M. F. Insana, "Linear system models for ultrasonic imaging: application to signal statistics," *IEEE Trans Ultrason Ferroelectr Freq Control,* vol. 50, pp. 642-54, Jun 2003.

[3] R. J. Zemp, M. D. Parry, C. K. Abbey, and M. F. Insana, "Detection performance theory for ultrasound imaging systems," *IEEE Trans Med Imaging,* vol. 24, pp. 300-10, Mar 2005.

[4] C. K. Abbey, N. Q. Nguyen, and M. F. Insana, "Optimal beamforming in ultrasound using the ideal observer," *IEEE Trans Ultrason Ferroelectr Freq Control,* vol. 57, pp. 1782-96, Aug 2010.

[5] C. K. Abbey, N. Q. Nguyen, and M. F. Insana, "Effects of Frequency and Bandwidth on Diagnostic Information Transfer in Ultrasonic B-Mode Imaging," *In Press at IEEE-TUFFC,* vol. TDB, 2012 2012.

[6] N. Q. Nguyen, C. K. Abbey, and M. F. Insana, "An adaptive filter to approximate the Bayesian strategy for sonographic beamforming," *IEEE Trans Med Imaging,* vol. 30, pp. 28-37, Jan 2011.

[7] J. A. Zagzebski, *Essentials of ultrasound physics*. St. Louis: Mosby, 1996.

[8] ISO-10993-1, "Biological Evaluation of Medical Devices Part 1: Evaluation and Testing," 2003.

[9] W. D. O'Brien, Jr., J. G. Abbott, M. E. Stratmeyer, G. R. Harris, M. E. Schafer, T. A. Siddiqi, C. R. Merritt, F. A. Duck, and P. J. Bendick, "Acoustic output upper limits proposition: should upper limits be retained?," *J Ultrasound Med,* vol. 21, pp. 1335-41, Dec 2002.

[10] NCRP, "NCRP Report No. 140. Exposure Criteria for Medical Diagnostic Ultrasound: II. Criteria Based on all Known Mechanisms," N. C. o. R. P. a. Measurements, Ed. Bethesda, MD: National Council on Radiation Protection and Measurements, 2002.

[11] S. W. Smith, R. F. Wagner, J. M. Sandrik, and H. Lopez, " Low contrast detectability and contrast/detail analysis in medical ultrasound," *IEEE Trans. Sonics Ultrason.,* vol. 30, pp. 164-173, 1983.